

On the rarity of rocket-driven Penrose extraction in Kerr spacetime*

An T. Le[†]

College of Engineering and Computer Sciences, VinUniversity, Hanoi, Vietnam

Center for Environmental Intelligence, VinUniversity, Hanoi, Vietnam and

Intelligent Autonomous Systems, TU Darmstadt, Germany

(Dated: January 28, 2026)

We present a Monte Carlo study of energy extraction from rotating (Kerr) black holes via the Penrose process using rocket propulsion, framing controlled exhaust as a constrained negative-energy injection problem that complements prior bounds on collisional mechanisms. Through over 112,000 trajectory simulations in the main experimental phases plus 140,000 additional trajectories for spin-threshold characterization (Table VII), we establish *sharp constraints* on when Penrose extraction with escape to infinity succeeds. The mechanism requires that exhaust ejected inside the ergosphere carries negative Killing energy $E_{\text{ex}} < 0$, which becomes kinematically accessible only for sufficiently deep ergosphere penetration (near periapsis) together with ejecta that is sufficiently “sub-rotating” relative to frame dragging (typically corresponding to negative angular momentum for the exhaust), and at ultra-relativistic exhaust speed; the spacecraft must then retain enough angular momentum to escape rather than plunge. Within our baseline steering prescriptions and sampled initial-condition domains, successful extraction with escape is statistically rare ($\sim 1\%$ in broad parameter scans), requires high spin (in a dedicated sweep with baseline $v_e = 0.95c$ and $\delta m = 0.3$, we observed no successes for $a/M \leq 0.88$ and a nonzero rate at $a/M = 0.89$, implying an empirical threshold $0.88 < a_{\text{crit}}/M \lesssim 0.89$ for this protocol), and exhibits a sharp onset in exhaust velocity around $v_e \approx 0.91\text{--}0.92c$. When these stringent conditions are met—i.e., conditioning on a narrow sweet-spot region (prograde flyby with specific energy $E_0 \approx 1.2$, specific angular momentum $L_z \approx 3.0$, and $v_e = 0.98c$)—success rates can reach 88.5% for $\delta m = 0.4$, but this represents a highly tuned extraction window rather than generic behavior. Single-impulse thrust at periapsis achieves $\eta_{\text{cum}} \approx 19\%$, while continuous thrust yields only $\sim 2\text{--}4\%$ due to path-averaging over regions where $|E_{\text{ex}}|$ is small. These constraints quantify the fine-tuning required for rocket-driven (material) Penrose extraction and are consistent with why electromagnetic mechanisms are generally considered the dominant channel for astrophysical black hole energy extraction. Simulation code is available at https://github.com/anindex/penrose_process.

I. INTRODUCTION

The extraction of energy from rotating black holes stands as one of the most remarkable predictions of general relativity. In 1969, Roger Penrose proposed a mechanism whereby particles entering the ergosphere of a Kerr black hole could split, with one fragment falling into the horizon carrying negative energy at infinity while the other escapes with energy exceeding that of the original particle [1]. This *Penrose process* demonstrates that up to 29% of a black hole’s mass—the extractable rotational energy above the irreducible mass—is in principle accessible [2, 3].

The theoretical elegance of the Penrose process has inspired decades of research into its variants and astrophysical manifestations. Wald [4] established the maximum single-decay efficiency of $\sim 20.7\%$ for an extremal Kerr black hole, while Piran, Shaham, and Katz [5] showed that particle *collisions* in the ergosphere could achieve substantially higher center-of-mass energies. This collisional Penrose process was later shown by Bañados, Silk, and West [6] to yield arbitrarily high center-of-mass ener-

gies near extremal horizons, though practical efficiencies are limited by gravitational redshift of escaping debris [7–9]. Leiderschneider and Piran [10] systematically characterized the maximal efficiency of the collisional process.

In astrophysical contexts, electromagnetic variants of energy extraction have proven more observationally relevant. The Blandford-Znajek mechanism [11] extracts rotational energy through magnetic field lines threading an accretion disk, powering the relativistic jets observed in active galactic nuclei and quasars [12]. More recently, Comisso and Asenjo [13] demonstrated that magnetic reconnection in the ergosphere provides an efficient Penrose-like mechanism, potentially explaining the rapid variability of high-energy emission from supermassive black holes. Koide and Arai [14] had earlier explored similar magnetic reconnection scenarios numerically.

Despite this rich theoretical landscape, a fundamental question remains largely unexplored: *How fine-tuned must conditions be for successful Penrose extraction with escape to infinity?* The classical Penrose process requires precisely tuned initial conditions—the decaying particle must enter the ergosphere on a trajectory that (i) penetrates deep enough for negative-energy states to be accessible (the exhaust must be ejected where frame-dragging is strong), (ii) does not plunge into the horizon, and (iii) allows the positive-energy fragment to escape with sufficient angular momentum. This narrow viable region in

* Corresponding author: An T. Le, an.lt@vinuni.edu.vn; an@robot-learning.de

† <https://vinuni.edu.vn/people/le-thai-an/>

parameter space has been noted qualitatively [15, 16], but no systematic statistical characterization exists to quantify *how rare* success is or *what parameter thresholds* govern extraction.

This paper addresses this gap by studying the Penrose process via *rocket propulsion*—a spacecraft that ejects mass (exhaust) inside the ergosphere, analogous to the classical particle decay but with thrust direction and magnitude allowed to vary under explicit steering prescriptions. We provide a *computational feasibility map* for rocket-like Penrose extraction, establishing quantitative thresholds, efficiencies, and success probabilities across large parameter sweeps. This formulation offers three advantages. First, it connects the abstract Penrose process to a concrete engineering scenario, clarifying which physical parameters govern extraction. Second, it enables Monte Carlo exploration of the initial condition space, quantifying the statistical rarity of successful extraction with escape. Third, it permits comparison of thrust strategies (impulsive vs. continuous), revealing path-averaging effects that reduce efficiency in extended maneuvers. The novelty of this work lies not in the existence of the Penrose process, but in providing *quantified success rates and parameter thresholds* under a rocket-propulsion control model, together with a thrust-profile comparison and a constrained optimality argument.

Our central finding is a set of *constraint results*: even allowing thrust direction and magnitude to vary under our steering prescriptions, successful Penrose extraction with spacecraft escape requires (i) high spin (no successes for $a/M \leq 0.88$ in our baseline sweep, constraining $0.88 < a_{\text{crit}}/M \lesssim 0.89$), (ii) ultra-relativistic exhaust velocity $v_e \gtrsim 0.91c$ (onset around 0.91 – $0.92c$), and (iii) carefully tuned initial conditions within a narrow “sweet spot.” Outside these constraints, extraction generically fails ($\sim 1\%$ success in broad parameter scans). The high success rates achievable under optimal conditions (88% at $v_e = 0.98c$, $\delta m = 0.4$) represent the limiting case of maximum fine-tuning, not typical behavior. Continuous thrust yields only ~ 10 – 20% of the single-impulse cumulative efficiency ($\eta_{\text{cum}} \sim 2$ – 4% versus $\sim 19\%$) due to path-averaging over the ergosphere transit, where $|E_{\text{ex}}|$ varies from near-zero at the boundary to maximally negative at periapsis, reinforcing that thrust timing is critical. We report all results with Clopper-Pearson exact confidence intervals for proportions and BCa bootstrap for efficiency metrics.

The paper is organized as follows. Section II reviews Kerr spacetime geometry. Sections III–V summarize the classical, collisional, and continuous Penrose processes. Sections VI–VII present the Hamiltonian formulation and thrust model. Section VIII describes numerical methods. Section IX presents our results with discussion. Section X then provides a simple optimal-allocation argument explaining why periapsis-impulse ejection is near-optimal for a fixed fuel budget. Finally, Section XI summarizes implications.

II. PROBLEM SETTING: KERR SPACETIME

To make the control and energetics statements precise, we begin by fixing notation for Kerr geometry, the ergosphere, and the conserved quantities used throughout.

We consider a rotating (Kerr) black hole of mass M and angular momentum $J = aM$, where $0 \leq a \leq M$ is the spin parameter. In Boyer-Lindquist coordinates (t, r, θ, ϕ) , the Kerr metric takes the form

$$ds^2 = - \left(1 - \frac{2Mr}{\Sigma} \right) dt^2 - \frac{4Mar \sin^2 \theta}{\Sigma} dt d\phi + \frac{\Sigma}{\Delta} dr^2 + \Sigma d\theta^2 + \frac{A \sin^2 \theta}{\Sigma} d\phi^2, \quad (1)$$

where

$$\Sigma = r^2 + a^2 \cos^2 \theta, \quad (2)$$

$$\Delta = r^2 - 2Mr + a^2, \quad (3)$$

$$A = (r^2 + a^2)^2 - a^2 \Delta \sin^2 \theta. \quad (4)$$

The event horizon is located at

$$r_+ = M + \sqrt{M^2 - a^2}, \quad (5)$$

which exists for $a \leq M$. The extremal limit $a = M$ corresponds to a maximally rotating black hole with $r_+ = M$.

A. The Ergosphere

The stationary limit surface (outer boundary of the ergosphere) is defined by $g_{tt} = 0$, yielding

$$r_{\text{erg}}(\theta) = M + \sqrt{M^2 - a^2 \cos^2 \theta}. \quad (6)$$

At the equatorial plane ($\theta = \pi/2$), we have $r_{\text{erg}} = 2M$ for all values of spin. The ergosphere is the region $r_+ < r < r_{\text{erg}}(\theta)$ where the Killing vector $\xi^\mu = (\partial/\partial t)^\mu$ becomes spacelike, meaning no observer can remain stationary.

Inside the ergosphere, all physical observers are dragged in the direction of black hole rotation. The angular velocity of frame dragging is

$$\omega = -\frac{g_{t\phi}}{g_{\phi\phi}} = \frac{2Mar}{A}. \quad (7)$$

This frame-dragging is central to energy extraction via the Penrose mechanism.

B. Constants of Motion

The Kerr spacetime admits two Killing vectors: $\xi^\mu = (\partial/\partial t)^\mu$ (stationarity) and $\psi^\mu = (\partial/\partial\phi)^\mu$ (axisymmetry). For geodesic motion, these yield conserved quantities:

$$E = -p_t = -g_{t\mu} p^\mu, \quad (8)$$

$$L_z = p_\phi = g_{\phi\mu} p^\mu, \quad (9)$$

where E is the energy at infinity and L_z is the azimuthal angular momentum.

III. CLASSICAL PENROSE PROCESS

The original Penrose process [1] provides a mechanism to extract rotational energy from a Kerr black hole using particle decay.

A. Physical Mechanism

Consider an incident particle with 4-momentum p_0^μ and energy $E_0 > 0$ entering the ergosphere. Inside the ergosphere, the particle undergoes a decay:

$$\text{particle}_0 \rightarrow \text{particle}_1 + \text{particle}_2. \quad (10)$$

Conservation of 4-momentum requires

$$p_0^\mu = p_1^\mu + p_2^\mu. \quad (11)$$

Contracting with the Killing vector $\xi_\mu = (\partial/\partial t)_\mu$:

$$E_0 = E_1 + E_2. \quad (12)$$

The key insight is that inside the ergosphere, time-like worldlines can have $E < 0$ (negative energy at infinity) while remaining physical. Specifically, if particle 2 is ejected with large retrograde angular momentum (opposing the black hole rotation), it can achieve $E_2 < 0$. Particle 1 then escapes with

$$E_1 = E_0 - E_2 > E_0, \quad (13)$$

extracting energy from the black hole.

B. Efficiency Limits

Two distinct efficiency bounds govern energy extraction. The *total extractable rotational energy* of a Kerr black hole is [2]:

$$\eta_{\text{rot}} = 1 - \sqrt{\frac{1 + \sqrt{1 - (a/M)^2}}{2}}, \quad (14)$$

which gives $\eta_{\text{rot}} \approx 29.3\%$ for an extremal black hole ($a = M$). This represents the thermodynamic limit on cumulative extraction via repeated processes.

The *single-decay efficiency* was bounded by Wald [4]:

$$\eta_{\text{Wald}} \approx 20.7\% \quad (\text{extremal Kerr}), \quad (15)$$

which corresponds (for an incident particle from rest at infinity) to a maximum fractional gain $(E_1 - E_0)/E_0 \simeq 0.207$ for the escaping fragment. Our single-impulse results should be compared to this bound, while cumulative processes may approach the rotational bound through multiple extractions.

C. Conditions for Energy Extraction

For successful energy extraction, the escaping particle must satisfy:

1. The decay occurs inside the ergosphere: $r_+ < r < r_{\text{erg}}$.
2. The “waste” particle has negative energy: $E_2 < 0$.
3. The escaping particle reaches infinity: trajectory is unbound with $E_1 > 0$.

A necessary condition for $E_2 < 0$ is that the fragment is created inside the ergosphere and carries sufficiently negative angular momentum (equivalently, sufficiently “sub-rotating” angular velocity relative to frame dragging). Writing $p^\mu = mu^\mu$ and $u^\phi = \Omega u^t$ with $\Omega := d\phi/dt$, we have

$$\frac{E}{m} = -u_t = -u^t (g_{tt} + g_{t\phi}\Omega). \quad (16)$$

For future-directed motion $u^t > 0$, the condition $E < 0$ is therefore

$$g_{tt} + g_{t\phi}\Omega > 0 \iff \Omega < -\frac{g_{tt}}{g_{t\phi}} \quad (g_{t\phi} < 0). \quad (17)$$

Outside the ergosphere, $g_{tt} < 0$ and the Killing vector ∂_t is timelike, implying $E > 0$ for any future-directed time-like worldline; thus negative-energy states are confined to the ergosphere. Note that even inside the ergosphere, frame dragging enforces $\Omega \in (\Omega_-, \Omega_+)$ with $\Omega_\pm > 0$, where

$$\Omega_\pm = \frac{-g_{t\phi} \pm \sqrt{g_{t\phi}^2 - g_{tt}g_{\phi\phi}}}{g_{\phi\phi}}. \quad (18)$$

Hence “retrograde” here refers to negative $L_z = p_\phi$ (or retrograde motion relative to a locally non-rotating frame), not to $u^\phi < 0$ in Boyer–Lindquist coordinates.

IV. COLLISIONAL PENROSE PROCESS

The collisional Penrose process [5, 7] enhances energy extraction through particle collisions rather than spontaneous decay.

A. Setup

Two particles are sent into the ergosphere on carefully chosen trajectories designed to collide near the horizon:

$$\text{particle}_1 + \text{particle}_2 \rightarrow \text{particle}_3 + \text{particle}_4. \quad (19)$$

The center-of-mass energy in the collision can be significantly boosted due to the extreme gravitational blueshift near the horizon.

B. Enhanced Efficiency

The key advantage of the collisional process is the center-of-mass energy available for the collision. For particles meeting near the horizon, the Lorentz factor in the local frame can become arbitrarily large. If one particle is on a marginally bound orbit with critical angular momentum L_c , the center-of-mass energy diverges as $r \rightarrow r_+$ (for extremal Kerr, $a = M$):

$$\sqrt{s} \propto \frac{1}{\sqrt{r - r_+}} \quad \text{as} \quad r \rightarrow r_+. \quad (20)$$

However, practical considerations (gravitational redshift of escaping particles, astrophysical particle fluxes) limit the actual energy gain. The Bañados-Silk-West mechanism [6] showed that for extremal Kerr black holes, arbitrary center-of-mass energies are possible in principle.

While collisional mechanisms can access extreme local energies, practical extraction with escape remains sensitive to kinematic tuning and redshift limitations. Motivated by this fine-tuning, we now replace the discrete “split”/collision picture with a controlled, variable-mass model: a spacecraft that ejects exhaust inside the ergosphere.

V. CONTINUOUS PENROSE PROCESS

We introduce a *continuous* variant of the Penrose process where a spacecraft equipped with a rocket engine operates inside the ergosphere, continuously expelling exhaust rather than undergoing discrete decay events.

A. Physical Concept

A spacecraft with initial rest mass m_0 and energy $E_0 > 1$ (unbound) enters the ergosphere on a *prograde flyby orbit* (angular momentum $L_z > 0$, co-rotating with the black hole). The orbit is chosen such that its periapsis lies inside the ergosphere. While passing through the ergosphere near periapsis, the spacecraft activates a rocket engine that:

1. Ejects mass at exhaust velocity v_e (in the spacecraft’s rest frame).
2. Chooses a thrust orientation such that the exhaust carries sufficiently negative angular momentum (equivalently, sufficiently “sub-rotating” angular velocity relative to the locally non-rotating frame) to access negative-energy states.
3. When this ejection occurs inside the ergosphere, the exhaust can have negative Killing energy at infinity ($E_{\text{ex}} < 0$), transferring energy to the remaining spacecraft.

Conceptually, each infinitesimal exhaust element plays the role of the negative-energy fragment in the classical split, while the remaining spacecraft plays the role of the escaping fragment; the rocket engine provides control over the split direction and timing. Throughout this paper, by “retrograde exhaust” we mean negative exhaust angular momentum (or retrograde motion relative to a locally non-rotating/ZAMO frame); due to frame dragging, future-directed timelike worldlines inside the ergosphere still have positive coordinate angular velocity.

The ejection of negative-energy exhaust results in the spacecraft gaining energy at infinity, emerging from the flyby with $E_f > E_0$. This is the continuous Penrose process: many infinitesimal mass ejections, each carrying away negative Killing energy.

Critical insight: In our parameter sweeps, successful extraction with escape arises from *prograde, initially unbound* flybys ($L_z > 0$, $E > 1$). Retrograde ($L_z < 0$) or initially bound ($E < 1$) initial conditions did not yield successful extraction with escape in our sampled domain, consistent with their more restrictive turning-point structure for deep ergosphere transits.

B. Advantages Over Classical Process

The continuous process offers practical advantages: rocket propulsion is well-understood technology; thrust magnitude and direction can be modulated; and active propulsion allows trajectory control to remain in the ergosphere and avoid capture.

C. Definition of Penrose Success

We define a *Penrose success event* as the conjunction of two conditions:

$$\mathcal{S} := (E_{\text{ex}} < 0 \text{ during at least one burn}) \wedge (\text{spacecraft escapes to infinity}). \quad (21)$$

Operationally, *escape* is diagnosed when the spacecraft reaches $r > 50M$ with outward radial velocity $dr/d\tau > 0$ and specific energy $E/m > 1$. *Capture* is diagnosed when $r < r_+ + 0.02M$ (horizon approach) or when integration fails due to stiffness near the horizon. Integration failures (11.2% of samples in our sweeps) are conservatively counted as captures.

For future-directed timelike exhaust, $E_{\text{ex}} < 0$ implies the exhaust cannot reach infinity: outside the ergosphere the stationary Killing vector ∂_t is timelike, forcing $E = -p_t \geq 0$ for any physical worldline. Negative-energy exhaust is therefore confined to the ergoregion and cannot escape to infinity. In our simulations we also explicitly verify exhaust capture (Sec. VII D), so counted success events correspond to both spacecraft energy gain and black-hole rotational energy decrease.

This definition ensures that “Penrose success” requires both the extraction signature ($E_{\text{ex}} < 0$) and the ability to carry the extracted energy to infinity. Achieving $E_{\text{ex}} < 0$ alone is insufficient—the spacecraft must also navigate out of the ergosphere without plunging. Under our throttle and sign-selection policy, all runs satisfying Eq. (19) also satisfy $\Delta E > 0$; we verified this empirically, so “ $E_{\text{ex}} < 0$ during at least one burn” is equivalent to net extraction in our dataset.

D. Efficiency Metrics

We define the *instantaneous efficiency* $\eta_{\text{inst}} = dE/d(-m)$, where $\eta_{\text{inst}} > 1$ indicates rest-mass break-even is exceeded. However, this alone does not prove Penrose extraction—a direct signature is negative exhaust Killing energy $E_{\text{ex}} < 0$ inside the ergosphere.

The *cumulative efficiency* over the maneuver is:

$$\eta_{\text{cum}} = \frac{E_f - E_0}{m_0 - m_f} = \frac{\Delta E}{\Delta m}. \quad (22)$$

For later parameter sweeps we report propellant expenditure via the ejected rocket mass fraction

$$\delta m := \frac{m_0 - m_f}{m_0}, \quad (23)$$

so that $\Delta m = m_0 - m_f = \delta m m_0$.

For relativistic exhaust velocity v_e with Lorentz factor $\gamma_e = 1/\sqrt{1 - v_e^2}$, the exhaust rest mass is $\delta\mu = \Delta m/\gamma_e$. The cumulative efficiency η_{cum} (Eq. 22) measures energy gain per unit *rocket mass lost*; for reference, one may also define a rest-mass efficiency $\eta_{\text{rest}} = \Delta E/\delta\mu = \gamma_e \cdot \eta_{\text{cum}}$ normalized to exhaust rest mass. Throughout this paper, we report η_{cum} unless otherwise noted, as it directly reflects the propellant budget expended by the spacecraft. This metric is distinct from Wald’s classic single-decay efficiency (a fractional gain normalized to the parent particle energy at infinity); we quote $\eta_{\text{Wald}} \approx 20.7\%$ for extremal Kerr as a familiar reference scale [4].

E. Analytic Velocity Threshold

A key prediction of our Monte Carlo study is a sharp velocity threshold near $v_e \approx 0.91\text{--}0.92c$, below which Penrose extraction largely fails. We now connect this transition to the local requirement that the *exhaust* (not the spacecraft) attain negative Killing energy.

For convenience we preview here the exact exhaust energy expression derived later in Sec. VII D:

$$E_{\text{ex}} = -\gamma_e(u_t - v_e s_t), \quad (24)$$

where $u_t = g_{t\mu}u^\mu$ is the covariant time component of the spacecraft 4-velocity and $s_t = g_{t\mu}s^\mu$ is the covariant time component of the unit spacelike *thrust* direction (the exhaust is emitted opposite to s^μ).

Negative-energy exhaust requires

$$E_{\text{ex}} < 0 \iff u_t - v_e s_t > 0. \quad (25)$$

For the unbound, escaping trajectories of interest we have $E/m = -u_t > 1$, hence $u_t < 0$. Equation (25) then implies a simple but important sign constraint: the thrust direction must satisfy $s_t < 0$ so that the $-v_e s_t$ term can overcome the negative u_t . In our setup, this is achieved by selecting thrust orientations that eject exhaust sufficiently *retrograde* in the local rest frame—the standard requirement for accessing negative-energy states inside the ergosphere.

When $u_t < 0$ and $s_t < 0$, Eq. (25) becomes a *lower bound* on exhaust speed:

$$v_e > v_e^{\text{crit}} := \frac{|u_t|}{|s_t|}, \quad (26)$$

with u_t and s_t evaluated at the burn event. This makes the origin of the “phase transition” transparent: as v_e increases, the set of spacetime points and thrust angles satisfying $v_e > v_e^{\text{crit}}$ (hence $E_{\text{ex}} < 0$) expands rapidly.

Evaluating Eq. (26) at periapsis for representative sweet-spot states ($a/M = 0.95$, $r_p \approx 1.5M$, $E_0 \approx 1.2$, $L_z \approx 3.0$) yields $v_e^{\text{crit}} \approx 0.85\text{--}0.92c$, depending on the orbital phase and steering angle. This estimate is consistent with the Monte Carlo observation (Fig. 5) that success rates transition sharply around $v_e \approx 0.91\text{--}0.92c$: below this value, only rare geometries achieve $E_{\text{ex}} < 0$ while retaining escape; above it, negative-energy exhaust becomes robust over a wide range of periapsis configurations.

Important caveat: The threshold $v_e \approx 0.91\text{--}0.92c$ is *not* a universal Kerr-invariant constant. It is an empirical threshold specific to our baseline sweet-spot distribution (Gaussian sampling around $E_0 = 1.22$, $L_z = 3.05$) and our greedy thrust policy (maximize instantaneous $-dp_t/d\tau$). Different orbit families, steering laws, or spin parameters will yield different critical velocities. The threshold is thus a geometric constraint arising from the competition between the spacecraft’s prograde motion and the retrograde exhaust required to tap the black hole’s rotational energy, evaluated for a particular class of trajectories.

We now formalize this controlled-ejection Penrose variant as a variable-mass, forced trajectory problem in Kerr spacetime.

VI. MATHEMATICAL FORMULATION

We now present the Hamiltonian formulation for the continuous Penrose process in Kerr spacetime.

A. Equatorial Restriction

For simplicity, we restrict to equatorial motion ($\theta = \pi/2$, $p_\theta = 0$). The dynamics reduce from 8 to 6 dimen-

sions. At the equator:

$$\Sigma = r^2, \quad (27)$$

$$\Delta = r^2 - 2Mr + a^2, \quad (28)$$

$$g_{tt} = -\left(1 - \frac{2M}{r}\right), \quad (29)$$

$$g_{t\phi} = -\frac{2Ma}{r}, \quad (30)$$

$$g_{rr} = \frac{r^2}{\Delta}, \quad (31)$$

$$g_{\phi\phi} = r^2 + a^2 + \frac{2Ma^2}{r}. \quad (32)$$

B. State Variables

The state vector for the spacecraft is

$$\mathbf{y} = (r, \phi, p_t, p_r, p_\phi, m), \quad (33)$$

where:

- r : Boyer-Lindquist radial coordinate
- ϕ : Azimuthal angle
- p_t : Covariant time momentum (energy: $E = -p_t$)
- p_r : Covariant radial momentum
- p_ϕ : Covariant azimuthal momentum (angular momentum: $L_z = p_\phi$)
- m : Rest mass (evolving due to propellant consumption)

C. Mass-Shell Constraint

The spacecraft 4-momentum must satisfy the mass-shell condition:

$$g^{\mu\nu} p_\mu p_\nu = -m^2. \quad (34)$$

Expanding at the equator:

$$g^{tt} p_t^2 + 2g^{t\phi} p_t p_\phi + g^{rr} p_r^2 + g^{\phi\phi} p_\phi^2 = -m^2. \quad (35)$$

This constrains the relationship between p_t , p_r , and p_ϕ for given m .

D. Hamiltonian

The Hamiltonian for a free particle is

$$\mathcal{H} = \frac{1}{2} g^{\mu\nu} p_\mu p_\nu = \frac{1}{2} (g^{tt} p_t^2 + 2g^{t\phi} p_t p_\phi + g^{rr} p_r^2 + g^{\phi\phi} p_\phi^2). \quad (36)$$

For massive particles with $p_\mu = mu_\mu$, the mass-shell constraint gives $\mathcal{H} = -m^2/2$.

For evolution in proper time τ (rather than affine parameter), we define:

$$\mathcal{H}_\tau = \frac{1}{2m} (g^{\mu\nu} p_\mu p_\nu + m^2), \quad (37)$$

which satisfies $\mathcal{H}_\tau = 0$ on shell. Hamilton's equations in proper time are:

$$\frac{dr}{d\tau} = \frac{1}{m} \frac{\partial \mathcal{H}}{\partial p_r} = \frac{g^{rr} p_r}{m}, \quad (38)$$

$$\frac{d\phi}{d\tau} = \frac{1}{m} \frac{\partial \mathcal{H}}{\partial p_\phi} = \frac{g^{\phi\phi} p_\phi + g^{t\phi} p_t}{m}, \quad (39)$$

$$\frac{dp_t}{d\tau} = -\frac{1}{m} \frac{\partial \mathcal{H}}{\partial t} = 0, \quad (40)$$

$$\frac{dp_r}{d\tau} = -\frac{1}{m} \frac{\partial \mathcal{H}}{\partial r}, \quad (41)$$

$$\frac{dp_\phi}{d\tau} = -\frac{1}{m} \frac{\partial \mathcal{H}}{\partial \phi} = 0. \quad (42)$$

The $1/m$ factor ensures that the Equivalence Principle is respected when mass varies, i.e., the gravitational acceleration does not depend on the particle's mass. Note that $p_t = -E$ and $p_\phi = L_z$ are conserved for geodesic motion.

VII. THRUST MODEL AND EQUATIONS OF MOTION

A. Variable-Mass Rocket Dynamics

For a rocket with proper acceleration a_{prop} and exhaust velocity v_e , the mass evolution follows the relativistic rocket equation:

$$\frac{dm}{d\tau} = -\frac{T}{v_e}, \quad (43)$$

where $T = m \cdot a_{\text{prop}}$ is the thrust magnitude.

With v_e denoting the exhaust speed in the rocket rest frame and Lorentz factor $\gamma_e = 1/\sqrt{1 - v_e^2}$, the exhaust momentum per unit rest mass is $\gamma_e v_e$. However, the *effective exhaust velocity* in the rocket equation $T = v_{\text{eff}}(-dm/d\tau)$ is simply $v_{\text{eff}} = v_e$, because the rocket mass loss $dm = \gamma_e d\mu$ accounts for the exhaust mass-energy in the rocket rest frame (rest mass plus kinetic energy). Our implementation uses this convention throughout: thrust magnitude $T = v_e(-dm/d\tau)$.

The 4-force on the spacecraft is

$$f^\mu = \frac{dp^\mu}{d\tau} - u^\mu \frac{dm}{d\tau}, \quad (44)$$

where $u^\mu = p^\mu/m$ is the 4-velocity. The force must satisfy the orthogonality condition:

$$u_\mu f^\mu = 0, \quad (45)$$

ensuring that thrust does not change the mass-shell condition.

B. Thrust Direction

To maintain physically meaningful thrust magnitude, we construct thrust in an orthonormal rocket-rest basis $\{u^\mu, e_{(r)}^\mu, e_{(\phi)}^\mu\}$ satisfying $u_\mu e_{(i)}^\mu = 0$ and $e_{(i)\mu} e_{(j)}^\mu = \delta_{ij}$. The unit thrust direction is

$$s^\mu = \sin \alpha e_{(r)}^\mu + \sigma \cos \alpha e_{(\phi)}^\mu, \quad \sigma \in \{+1, -1\}, \quad (46)$$

and $f^\mu = T s^\mu$, enforcing both $u_\mu f^\mu = 0$ and $f_\mu f^\mu = +T^2$.

C. Optimal Thrust Selection

The azimuthal thrust sign (\pm) is chosen to maximize instantaneous energy gain:

$$\text{Choose sign}(\pm) \text{ to maximize } -\frac{dp_t}{d\tau}. \quad (47)$$

Since $E = -p_t$, this maximizes the rate of energy extraction.

D. Exact 4-Momentum Conservation

For exact energy accounting, we use 4-momentum conservation rather than approximate thrust models. When the rocket ejects exhaust of rest mass $\delta\mu$ with 4-velocity u_{ex}^μ , conservation requires:

$$p'_\mu = p_\mu - \delta\mu \cdot u_{\text{ex},\mu}, \quad (48)$$

where p'_μ is the new rocket 4-momentum. The exhaust 4-velocity is:

$$u_{\text{ex}}^\mu = \gamma_e (u^\mu - v_e s^\mu), \quad (49)$$

where s^μ is the unit spacelike *thrust direction* (the direction of the reaction force on the rocket) and $\gamma_e = 1/\sqrt{1-v_e^2}$. Since the exhaust is ejected opposite to the thrust, the minus sign ensures correct physics. The covariant exhaust 4-velocity is $u_{\text{ex},\mu} = g_{\mu\nu} u_{\text{ex}}^\nu$.

The exhaust Killing energy is:

$$E_{\text{ex}} = -u_{\text{ex},t} = -\gamma_e (u_t - v_e s_t). \quad (50)$$

Negative E_{ex} is the unambiguous signature of Penrose extraction: the exhaust carries negative energy into the black hole, extracting rotational energy from the hole.

For continuous thrust, the rates are:

$$\frac{dp_\mu}{d\tau} = -\frac{d\mu}{d\tau} \cdot u_{\text{ex},\mu}, \quad (51)$$

where $d\mu/d\tau$ is the exhaust rest-mass ejection rate. The relation between rocket mass loss and thrust magnitude is:

$$\frac{dm}{d\tau} = -\gamma_e \frac{d\mu}{d\tau}, \quad T = \gamma_e v_e \frac{d\mu}{d\tau} = v_e \left(-\frac{dm}{d\tau} \right). \quad (52)$$

Note that the “effective exhaust velocity” in the standard rocket equation $T = v_{\text{eff}}(-dm/d\tau)$ is simply $v_{\text{eff}} = v_e$, not $\gamma_e v_e$.

Energy conservation is then verified by:

$$\Delta E + \sum_i E_{\text{ex},i} \cdot \delta\mu_i = 0, \quad (53)$$

where the sum is over all thrust events. This relation is satisfied to machine precision in our simulations.

Interpretation caveat. The identity above is Killing-energy conservation at the burn events (rocket plus exhaust), and holds without evolving the exhaust geodesic. However, interpreting “negative E_{ex} implies black hole energy decrease” requires that the negative-energy exhaust actually falls into the hole rather than escaping. For exhaust with $E_{\text{ex}} < 0$, capture is kinematically required (negative-energy worldlines cannot reach infinity). When $E_{\text{ex}} \geq 0$, the exhaust may either escape or be captured depending on its trajectory; our code explicitly tracks this distinction via `verify_exhaust_capture_batch()`.

E. Full Equations of Motion

Between thrust events, the spacecraft follows geodesic Hamiltonian evolution (Eqs. 38–42). In continuous-thrust mode, we add the covariant momentum source implied by exact 4-momentum conservation with the exhaust:

$$\left(\frac{dp_\mu}{d\tau} \right)_{\text{thrust}} = -\frac{d\mu}{d\tau} u_{\text{ex},\mu}, \quad \frac{dm}{d\tau} = -\gamma_e \frac{d\mu}{d\tau}, \quad (54)$$

with $u_{\text{ex},\mu} = \gamma_e (u_\mu - v_e s_\mu)$ from Eq. 49. The full forced system can be written compactly as

$$\frac{dp_\mu}{d\tau} = \left(\frac{dp_\mu}{d\tau} \right)_{\text{geo}} + \left(\frac{dp_\mu}{d\tau} \right)_{\text{thrust}}, \quad (55)$$

where $(dp_t/d\tau)_{\text{geo}} = (dp_\phi/d\tau)_{\text{geo}} = 0$ and $(dp_r/d\tau)_{\text{geo}} = -(1/m) \partial \mathcal{H} / \partial r$ (Eq. 41). Position updates use $p^\mu = g^{\mu\nu} p_\nu$ and $dx^\mu/d\tau = p^\mu/m$. In impulsive-thrust mode, we apply the discrete version of Eq. 48 at the burn event and then resume geodesic evolution.

F. Throttle Function

Thrust is activated only inside the *extraction zone* where Penrose extraction ($E_{\text{ex}} < 0$) is achievable. The extraction limit radius $R_{\text{extraction}}$ is computed dynamically as the maximum radius where $E_{\text{ex}} < 0$ is geometrically possible given the current orbit parameters. We implement this using a smooth throttle function $\chi(r)$:

$$\chi(r) = \begin{cases} 0, & r \leq r_{\text{in}} \text{ or } r \geq r_{\text{out}} \\ S\left(\frac{r-r_{\text{in}}}{w}\right) [1 - S\left(\frac{r-r_{\text{out}}}{w}\right)], & \text{otherwise} \end{cases} \quad (56)$$

where $r_{\text{in}} := r_+ + \epsilon_{\text{in}}$ and $r_{\text{out}} := R_{\text{extraction}} - \epsilon_{\text{out}}$ enforce safety margins near the horizon and near the extraction boundary; $S(x)$ is a smoothstep function providing C^2 -continuous ramp transitions, and w controls the ramp width.

The smoothstep function is:

$$S(x) = \begin{cases} 0 & x \leq 0 \\ 6x^5 - 15x^4 + 10x^3 & 0 < x < 1 \\ 1 & x \geq 1 \end{cases} \quad (57)$$

G. Steering and Protocol Summary

Our Monte Carlo experiments use explicit steering prescriptions rather than solving a global optimal-control problem. For reproducibility, we summarize the protocol used in both impulse and continuous-thrust simulations:

- **Thrust modes.** (i) *Periapsis impulse*: a single burn is executed at the first periapsis passage, expending a prescribed ejected mass fraction δm . (ii) *Continuous thrust*: thrust is applied continuously while the throttle $\chi(r)$ is nonzero (Sec. VII F) until the fuel budget is expended or a termination event occurs (escape/capture/constraint failure).
- **Azimuthal sign selection.** At each burn event (impulse or continuous step) we choose the azimuthal sign $\sigma \in \{+1, -1\}$ to maximize instantaneous Killing-energy gain, i.e. to maximize $-dp_t/d\tau$ (Sec. VII C).
- **Radial steering (continuous mode).** The radial steering angle α is set by a PID controller targeting $r_{\text{set}} \sim 1.5M$ to extend ergosphere dwell time while avoiding horizon approach (Sec. VIII D).
- **Exact energy accounting and capture.** Burn updates use exact 4-momentum conservation with an explicit exhaust 4-velocity (Sec. VII D); we also verify whether exhaust is captured or escapes, which is necessary for interpreting $E_{\text{ex}} < 0$ as black-hole energy decrease.

VIII. NUMERICAL METHODS

We work in geometric units $G = c = M = 1$ and in the test-particle limit ($m_0 \ll M$), so that backreaction and self-force are negligible and the Kerr background remains fixed. We normalize the spacecraft's initial rest mass to $m_0 = 1$; reported energies E and angular momenta L_z are therefore dimensionless specific quantities (per unit initial rest mass). When mass varies, the instantaneous specific energy is $E/m = -u_t$, and we diagnose escape by $E/m > 1$ at large radius.

A. Solver Selection

For parameter sweeps (single-impulse trajectories), we use SciPy's DOP853 integrator (8th-order Dormand-Prince) with adaptive step control, achieving machine-precision conservation of Killing quantities during geodesic phases. For continuous-thrust simulations, we employ explicit Euler with timestep $\Delta\tau = 0.005M$ and mass-shell projection after each step (enabling transparent debugging of near-horizon physics and thrust events). The projection modifies p_r to satisfy $g^{\mu\nu}p_\mu p_\nu + m^2 = 0$ while preserving $E = -p_t$.

Integrator validation. We verified that DOP853, RK45, and Radau methods yield identical trajectory outcomes (escape vs. capture) for all tested initial conditions. The Euler integrator alone shows numerical drift for pure geodesics but is stabilized by mass-shell projection during thrust phases. Convergence tests confirm that success rates are stable across timesteps $\Delta\tau \in [0.002, 0.02]M$ when projection is applied (see Appendix A).

B. Termination Events

Integration terminates upon: horizon approach ($r < r_+ + 0.02M$), mass depletion ($m < 0.1$), constraint violation ($|\mathcal{C}| > 10^{-1}$), or escape ($r > 50M$ with $dr/dt > 0$ and $E/m > 1$).

C. Initial Conditions

Initial conditions must represent a valid geodesic. Given $(r_0, E_0, L_{z,0}, m_0)$ with $r_0 = 15M$ (outside the ergosphere, allowing infall to be geodesic), we set:

$$p_t^{(0)} = -E_0, \quad (58)$$

$$p_\phi^{(0)} = L_{z,0}, \quad (59)$$

$$p_r^{(0)} = -\sqrt{\frac{-(g^{tt}p_t^{(0)2} + 2g^{t\phi}p_t^{(0)}p_\phi^{(0)} + g^{\phi\phi}p_\phi^{(0)2} + m_0^2)}{g^{rr}}}, \quad (60)$$

where the negative sign for $p_r^{(0)}$ indicates an initially infalling trajectory (moving toward smaller r).

For the initial state to be physical (i.e., within the allowed region for geodesic motion), we require:

$$g^{tt}p_t^2 + 2g^{t\phi}p_t p_\phi + g^{\phi\phi}p_\phi^2 + m^2 < 0, \quad (61)$$

ensuring $p_r^2 > 0$ (real radial momentum).

D. Radial Controller

To extend ergosphere duration, a PID controller adjusts the radial steering angle: $\alpha = \text{clamp}[k_p(r_{\text{set}} - r) -$

$k_d \dot{r} + k_i \int (r_{\text{set}} - r) d\tau]$, with gains $k_p = 50$, $k_d = 30$, $k_i = 5$, maximum angle $\alpha_{\text{max}} = 60^\circ$, and target radius $r_{\text{set}} \sim 1.5M$.

IX. NUMERICAL RESULTS

We present systematic numerical experiments characterizing the Penrose process for prograde flyby orbits. Our central finding is that *successful energy extraction with spacecraft escape is statistically rare*, occurring in a narrow region of parameter space, but is rigorously verified when achieved. All simulations use geometric units $G = c = M = 1$.

Organization of results. Our analysis proceeds as follows: Sec. IX A validates numerical accuracy; Sec. IX B identifies the extraction window using orbit classification (Fig. 1); Sec. IX C quantifies success rates via Monte Carlo sampling (Tables I–III, Fig. 2); Sec. IX D compares thrust strategies (Table IV, Fig. 3); Sec. IX E examines spin dependence (Fig. 4); Sec. IX F characterizes the velocity phase transition (Tables V–VI, Figs. 5–6); and Sec. IX G synthesizes these findings.

A. Numerical Validation

Our implementation preserves the mass-shell constraint to $|\mathcal{C}|_{\text{max}} < 10^{-9}$ (single-impulse) and $< 10^{-6}$ (continuous thrust with projection). Future-directedness ($u^t > 0$) and timelike normalization are verified throughout. Energy conservation via exact 4-momentum conservation yields residuals $< 10^{-9}$. Detailed diagnostics are provided in Appendix A.

B. Extraction Window in Parameter Space

The key is using *prograde flyby orbits* satisfying: (1) $E_0 > 1$ (unbound), (2) periapsis $r_{\text{peri}} < r_{\text{erg}} = 2M$ (ergosphere penetration), and (3) negative-angular-momentum exhaust direction (retrograde in the local frame, enabling $E_{\text{ex}} < 0$).

For diagnostics and visualization (Figs. 1 and 4), we further classify ergosphere-penetrating flybys by periapsis depth. Let $\Delta r_{\text{erg}} := r_{\text{erg}} - r_+$ denote the equatorial ergosphere thickness. We call a trajectory *shallow* if its periapsis lies in the outer 30% of the ergosphere, $r_{\text{peri}} > r_{\text{erg}} - 0.3 \Delta r_{\text{erg}}$, and *deep* otherwise; deep-ergosphere flybys correspond to the region where negative-angular-momentum (retrograde-in-local-frame) exhaust can robustly attain $E_{\text{ex}} < 0$.

For $a/M = 0.95$, the viable region is remarkably narrow: specific energy $E_0 \in [1.15, 1.35]$ and specific angular momentum $L_z \in [2.9, 3.3]$, yielding periapsis at $r_{\text{peri}} \approx 1.5M$. Orbits outside this window fail: initially bound conditions ($E_0 < 1$) remain bound under our baseline burns; low L_z leads to capture; high L_z places peri-

apsis outside the ergosphere; retrograde orbits ($L_z < 0$) with $E < 1$ universally captured in our sampled domain. Figure 1 shows how orbit classification depends critically on spin: at $a/M = 0.70$, the deep ergosphere region is negligible (confined to a thin band), while at $a/M = 0.95$, it expands to dominate 44% of parameter space.

C. Statistical Ensemble Analysis

To quantify the rarity of successful extraction with escape, we performed Monte Carlo ensemble studies using Latin Hypercube sampling over the parameter space (E_0, L_z, a) .

Unless stated otherwise, the grid/LHS sweeps in this section use a *single impulsive burn applied at periapsis*. Continuous-thrust trajectories are analyzed separately in Sec. IX D.

Statistical methodology. Parameter space coverage uses deterministic grids for systematic exploration and Latin Hypercube sampling (LHS) for Monte Carlo validation. All confidence intervals for proportions use the Clopper-Pearson exact method [17], treating each tested initial condition as a Bernoulli trial; efficiency uncertainties use BCa bootstrap with 10^4 resamples [18]. Trajectories with integration failures (11.2%) are counted as captures in our conservative analysis (Table VIII).

1. Broad Parameter Study

We performed comprehensive parameter sweeps across the full (E_0, L_z) space for five spin values, with $E_0 \in [0.95, 2.0]$, $L_z \in [-3.0, 6.0]$, using an 80×80 grid (6400 samples per spin). This broad scan establishes the overall rarity of successful Penrose extraction. Table I summarizes the results.

TABLE I. Broad parameter sweep results ($N = 6,400$ samples per spin, $E_0 \in [0.95, 2.0]$, $L_z \in [-3.0, 6.0]$, $v_e = 0.95c$, $\delta m = 0.20$). All confidence intervals use the Clopper-Pearson exact method [17]. The Penrose rate quantifies trajectories achieving both $E_{\text{ex}} < 0$ and escape to infinity. Integration uses DOP853 (8th-order Dormand-Prince) with tolerances $\text{rtol} = 10^{-10}$, $\text{atol} = 10^{-12}$.

a/M	N	Escape	Penrose	95% CI
0.50	6400	8.11%	0.00%	[0.00%, 0.06%]
0.70	6400	8.34%	0.00%	[0.00%, 0.06%]
0.90	6400	13.94%	0.03%	[0.00%, 0.11%]
0.95	6400	19.52%	0.95%	[0.73%, 1.22%]
0.99	6400	27.22%	1.41%	[1.13%, 1.73%]

2. Spin Threshold Analysis

To precisely characterize the spin dependence, we performed a sweep over 14 spin val-

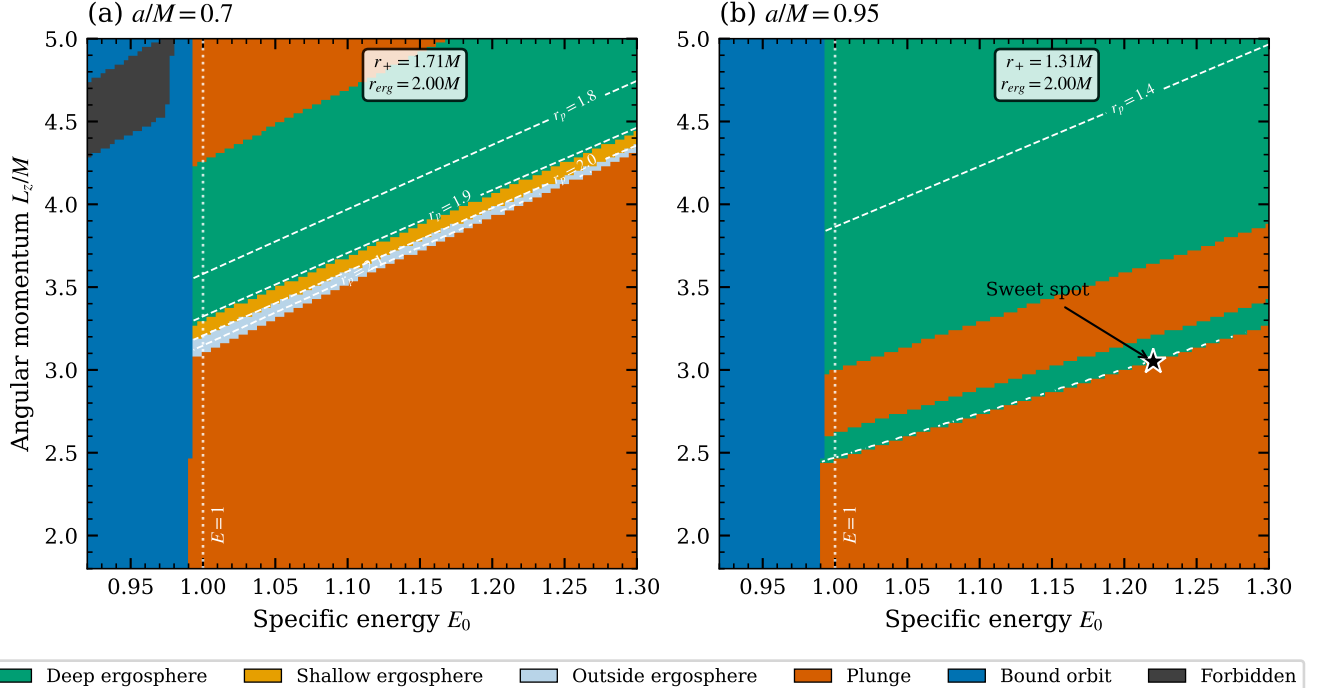


FIG. 1. Orbit classification in (E_0, L_z) parameter space comparing moderate and high spin. (a) $a/M = 0.70$: Six classification regions are present—forbidden (dark gray, inaccessible configurations), bound (blue, $E_0 < 1$), plunge (red, no turning point), outside ergosphere (light blue, $r_{\text{peri}} > r_{\text{erg}}$), shallow ergosphere (orange, outer 30% of ergosphere), and deep ergosphere (green, extraction zone). The deep ergosphere region is negligible due to the narrow ergosphere width ($0.29M$). (b) $a/M = 0.95$: Higher spin dramatically expands the deep ergosphere region (43.7% of parameter space) at the expense of shallow and outside regions (now absent). The wider ergosphere ($0.69M$) and stronger frame-dragging enable more trajectories to reach the extraction zone. Dashed white contours show constant periapsis r_p ; vertical dotted line marks $E_0 = 1$ (bound/unbound threshold). Star marker in panel (b) indicates the sweet spot $(E_0, L_z) = (1.22, 3.05)$.

ues: $a/M = 0.80, 0.81, \dots, 0.88$ plus $a/M \in \{0.89, 0.90, 0.92, 0.95, 0.99\}$, with 10,000 LHS samples per spin in the focused region. Table II shows the results.

TABLE II. Spin threshold analysis ($N = 10,000$ LHS samples per spin in focused region: $E_0 \in [1.1, 1.3]$, $L_z \in [2.5, 3.5]$; baseline thrust $v_e = 0.95c$, $\delta m = 0.3$). For compactness, the row $a/M \leq 0.88$ aggregates nine spins $a/M = 0.80, 0.81, \dots, 0.88$ (90,000 samples total). No successful extractions for $a/M \leq 0.88$ and nonzero rates at $a/M = 0.89$ constrain the practical threshold to $0.88 < a_{\text{crit}}/M \lesssim 0.89$.

a/M	N	Penrose Rate	95% CI
≤ 0.88	90,000	0.00%	[0.00%, 0.004%]
0.89	10,000	0.09%	[0.04%, 0.17%]
0.90	10,000	0.30%	[0.20%, 0.43%]
0.92	10,000	2.47%	[2.18%, 2.79%]
0.95	10,000	8.24%	[7.71%, 8.80%]
0.99	10,000	10.92%	[10.32%, 11.55%]

The key finding is that across this spin threshold sweep (140,000 additional LHS trajectories, separate from the main 112,000 in Table VII), *no successful Penrose extractions with escape* were observed for $a/M \leq 0.88$. Combined with the onset of successful extraction at $a/M = 0.89$, this constrains the practical spin thresh-

old for rocket-propelled Penrose extraction.

3. Focused Sweet-Spot Study

Restricting to the identified sweet spot ($E_0 \in [1.1, 1.4]$, $L_z \in [2.5, 3.8]$) using a 60×60 grid (3600 samples per spin) dramatically improves success rates:

TABLE III. Focused sweet-spot sweep results ($N = 3,600$ samples per spin, $E_0 \in [1.1, 1.4]$, $L_z \in [2.5, 3.8]$, $v_e = 0.95c$, $\delta m = 0.20$). The $\sim 12 \times$ increase in Penrose success rate ($0.95\% \rightarrow 11.19\%$ for $a/M = 0.95$) and $\sim 10 \times$ increase ($1.41\% \rightarrow 13.56\%$ for $a/M = 0.99$) confirm that successful extraction requires precise tuning of initial conditions. (Note: rates differ from Table II due to different sampling domains and methods.)

a/M	N	Escape	Penrose	95% CI
0.50	3600	0.00%	0.00%	[0.00%, 0.10%]
0.70	3600	2.78%	0.00%	[0.00%, 0.10%]
0.90	3600	18.64%	0.58%	[0.36%, 0.89%]
0.95	3600	26.33%	11.19%	[10.18%, 12.27%]
0.99	3600	65.14%	13.56%	[12.45%, 14.72%]

The $\sim 12 \times$ amplification in success rate (see Figure 2) confirms that precise initial condition tuning is essential.

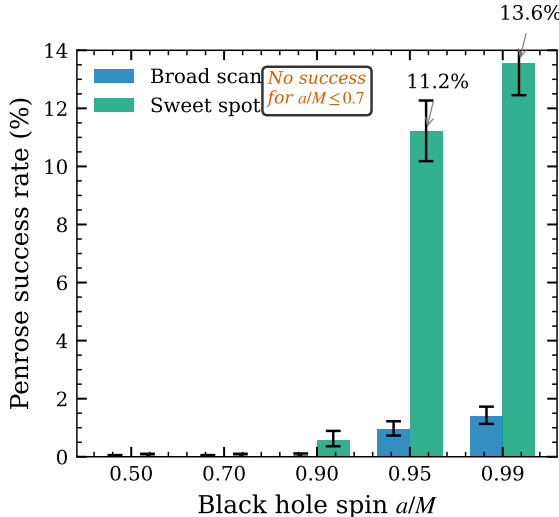


FIG. 2. Penrose success rate versus black hole spin from comprehensive parameter sweep: broad scan ($E_0 \in [0.95, 2.0]$, $L_z \in [-3.0, 6.0]$; blue, $N = 6,400$ per spin) and sweet-spot region ($E_0 \in [1.1, 1.4]$, $L_z \in [2.5, 3.8]$; green, $N = 3,600$ per spin). Error bars show 95% Clopper-Pearson exact confidence intervals. No successful extractions were observed for $a/M \leq 0.7$ across 12,800 trajectories. Focusing on the sweet spot yields amplification factors of $19 \times$ at $a/M = 0.9$, $12 \times$ at $a/M = 0.95$, and $10 \times$ at $a/M = 0.99$, demonstrating the essential role of precise initial condition tuning.

D. Thrust Strategy Comparison

We compare single-impulse and continuous thrust strategies using optimized configurations for each. Each strategy is reported at its own optimized configuration; the fuel fractions differ ($\delta m = 0.10$ for single impulse vs. $\delta m = 0.20$ for continuous) because continuous thrust required larger δm to robustly achieve escape under our controller. Table IV summarizes the results.

TABLE IV. Thrust strategy comparison for $a/M = 0.95$, $v_e = 0.95c$, $\delta m = 0.10$ (single impulse) and $\delta m = 0.20$ (continuous). Single impulse achieves $\eta_{\text{cum}} = 19.2\%$ (energy gain per rocket mass lost; Eq. 22). Continuous thrust with escape achieves both $E_{\text{ex}} < 0$ and escape but at reduced efficiency. Uncertainties represent standard deviations from parameter variations within the sweet spot.

Metric	Single Impulse	Cont. (Esc.)	Cont. (Capture)
(E_0, L_z)	$(1.20, +3.0)$	$(1.25, +3.1)$	$(1.20, +2.8)$
δm	0.10	0.20	0.20
ΔE	$+0.019 \pm 0.003$	$+0.004 \pm 0.003$	$+0.008 \pm 0.001$
η_{cum}	$19.2\% \pm 1.5\%$	$2.1\% \pm 1.3\%$	$3.9\% \pm 0.6\%$
$P(E_{\text{ex}} < 0)$	100%	$> 95\%$	$\sim 100\%$
Outcome	ESCAPE	ESCAPE	CAPTURE

Key findings: (1) Single impulse is optimal, achieving $\eta_{\text{cum}} \approx 19\%$ by concentrating fuel at periapsis. (2) Continuous thrust enables escape with reduced efficiency ($\sim 10\text{--}20\%$ of single-impulse). (3) Deeper periapsis increases $|E_{\text{ex}}|$ but also capture probability. (4) All config-

urations achieve $E_{\text{ex}} < 0$ for most thrust events. Figure 3 shows representative trajectories.

E. Spin Dependence

The extraction window depends sensitively on black hole spin. Our parameter sweep reveals that no successful extractions occur for $a/M \leq 0.7$ across 12,800 trajectories, while success rates climb rapidly for higher spins. Figure 4 illustrates the contraction of the extraction window with decreasing spin.

F. Thrust Parameter Sensitivity

A critical finding from our comprehensive sweep is the sharp dependence on exhaust velocity v_e . Our velocity analysis reveals a sharp onset (rapid transition region) around $v_e \approx 0.91\text{--}0.92c$ for our baseline sweet-spot distribution and greedy thrust policy: below this range, success is negligible regardless of other parameters, while above it success increases rapidly with both v_e and δm . Table V shows representative results for $a/M = 0.95$:

TABLE V. Thrust parameter sensitivity for $a/M = 0.95$ in the sweet-spot region centered at $(E_0 = 1.22, L_z = 3.05)$, with $N = 1,000$ initial conditions per configuration sampled from a Gaussian distribution centered at $(E_0, L_z) = (1.22, 3.05)$ with $\sigma_E = 0.03$, $\sigma_L = 0.08$. Penrose success rate as a function of exhaust velocity v_e and ejected mass fraction δm . A sharp onset (rapid transition region) occurs around $v_e \approx 0.91\text{--}0.92c$; below this threshold, success is negligible. Peak success of **88.5%** achieved at $v_e = 0.98c$, $\delta m = 0.4$. Corresponding cumulative efficiency trends are summarized in Fig. 5b.

v_e/c	$\delta m = 0.1$	$\delta m = 0.2$	$\delta m = 0.3$	$\delta m = 0.4$
0.80	0.0%	0.0%	0.0%	0.0%
0.90	1.0%	1.0%	1.0%	1.0%
0.95	54.1%	64.8%	71.7%	81.5%
0.98	59.4%	70.1%	77.5%	88.5%

For comparison, Table VI shows results for $a/M = 0.99$:

TABLE VI. Thrust parameter sensitivity for $a/M = 0.99$ in the sweet-spot region centered at $(E_0 = 1.22, L_z = 3.05)$, with $N = 1,000$ initial conditions per configuration (same Gaussian sampling protocol as Table V). Notably, $v_e = 0.90c$ yields 0% success (vs. 1% at $a/M = 0.95$), while $v_e = 0.98c$ achieves 86.3% success. The insensitivity to δm at this spin suggests a different phase-space geometry.

v_e/c	$\delta m = 0.1$	$\delta m = 0.2$	$\delta m = 0.3$	$\delta m = 0.4$
0.80	0.0%	0.0%	0.0%	0.0%
0.90	0.0%	0.0%	0.0%	0.0%
0.95	45.0%	45.0%	45.0%	45.0%
0.98	86.3%	86.3%	86.3%	86.3%

The cumulative efficiency η_{cum} (Eq. 22) increases with exhaust velocity: for $a/M = 0.95$ it rises from $\eta_{\text{cum}} \approx$

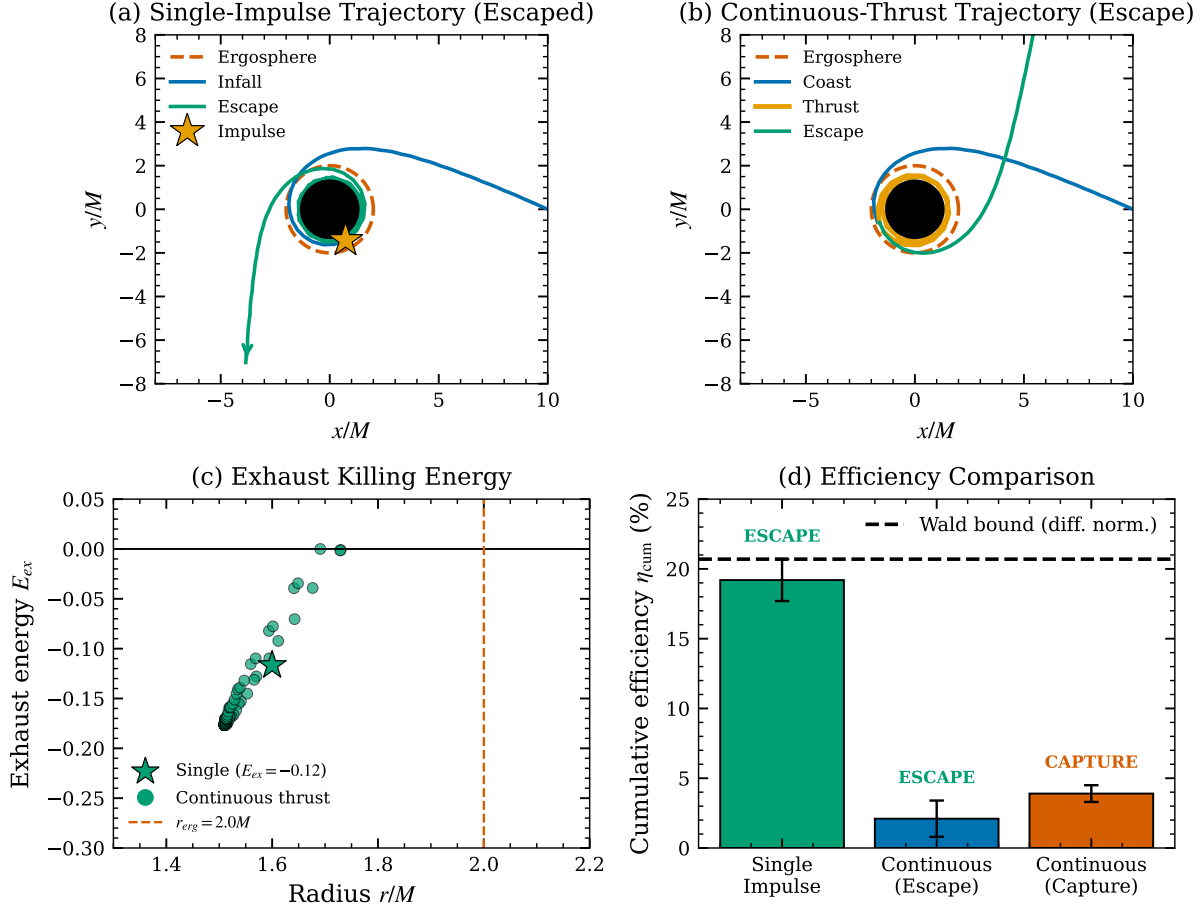


FIG. 3. Thrust strategy comparison at $a/M = 0.95$, $v_e = 0.95c$. (a) Single-impulse trajectory ($E_0 = 1.18$, $L_z = 2.92$): geodesic infall (blue), impulse at periapsis $r \approx 1.6M$ (orange star), geodesic escape (green); energy gain $\Delta E = +0.0073$. (b) Continuous thrust trajectory ($E_0 = 1.20$, $L_z = 3.0$): coasting infall (blue), sustained thrust with $\sim 34,000$ discrete events inside ergosphere (orange), escape (green); energy gain $\Delta E = +0.0025$. (c) Exhaust Killing energy E_{ex} versus radius: large star marks single-impulse event ($E_{\text{ex}} \approx -0.12$); small circles show continuous thrust events. For this representative trajectory, all events satisfy $E_{\text{ex}} < 0$; ensemble statistics (Table IV) show $P(E_{\text{ex}} < 0) > 95\%$. Dashed line marks ergosphere boundary ($r_{\text{erg}} = 2M$). (d) Cumulative efficiency: single impulse achieves $\eta_{\text{cum}} = 19.2\% \pm 1.5\%$ (Eq. 22); continuous thrust achieves $\sim 2\%$. Note: η_{cum} is normalized to rocket mass loss; Wald's 20.7% bound is normalized to incident particle energy E_0 and is not an upper bound on η_{cum} .

0.1–0.2% just above threshold ($v_e \approx 0.91$ – $0.92c$) to $\eta_{\text{cum}} \approx 5$ –7% at $v_e = 0.98c$ (Fig. 5b). At this spin, higher δm values increase *success rates* but *decrease* per-mass efficiency, presenting a design trade-off; at $a/M = 0.99$, success is comparatively insensitive to δm (Table VI). This velocity threshold establishes a fundamental constraint: *ultra-relativistic exhaust velocities are required* for practical Penrose propulsion. Within the thrust sensitivity study, combining higher exhaust velocity ($v_e = 0.98c$) with larger mass fraction ($\delta m = 0.4$) yields success rates of 88.5% for $a/M = 0.95$, compared to $\sim 54\%$ at $v_e = 0.95c$, $\delta m = 0.1$ in the same domain. Figure 5 visualizes this phase transition and the associated trade-off between success probability and per-mass efficiency.

To probe the asymptotic limit $v_e \rightarrow c$ —and test whether η_{cum} continues to grow once the phase transition is passed—we extend the same single-impulse sweet-

spot study by pushing the exhaust velocity into the ultra-relativistic regime, up to $v_e = 0.99999c$ ($\gamma \approx 224$). Figure 6 continues Fig. 5b and shows that the efficiency gain beyond $v_e \sim 0.99c$ is modest, approaching a plateau for this spin parameter.

G. Discussion

Figures 5 and 6 together show a two-stage dependence of material Penrose extraction on exhaust speed: a sharp onset of viable negative-energy ejection near $v_e \approx 0.91$ – $0.92c$, followed by diminishing efficiency gains as $v_e \rightarrow c$ once the threshold is passed. Our results confirm the analytic velocity threshold derived in Sec. V E. The sharp transition arises from the geometric requirement that retrograde exhaust momentum must overcome

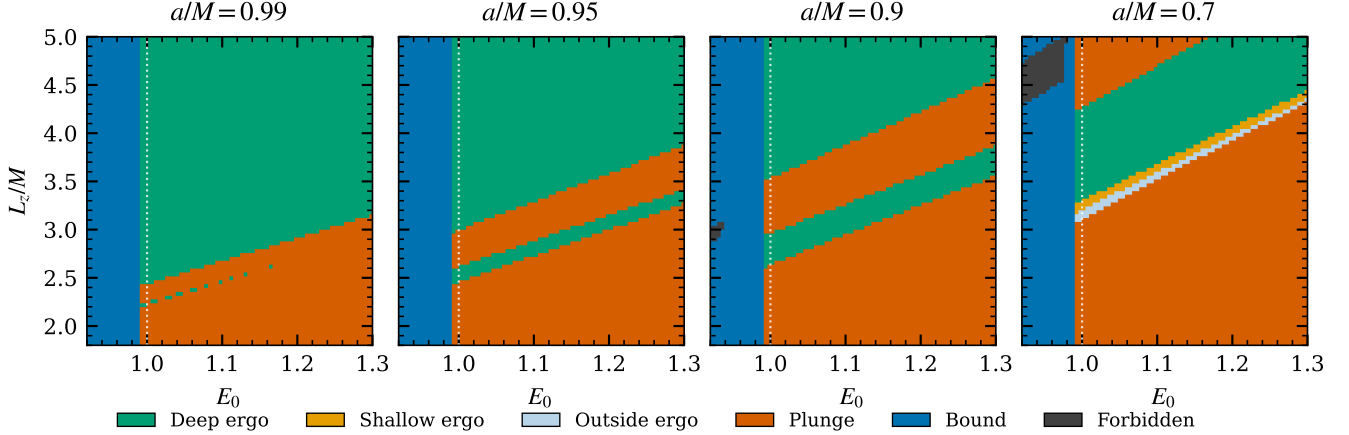


FIG. 4. Spin dependence of the extraction window. Panels show orbit classification in (E_0, L_z) space for $a/M = 0.99, 0.95, 0.9$, and 0.7 (left to right). Color coding follows Fig. 1: green indicates deep ergosphere flyby, orange shallow ergosphere, light blue outside ergosphere, red plunge, blue bound ($E_0 < 1$), and gray forbidden. The deep ergosphere region (extraction zone) expands dramatically with increasing spin: from negligible at $a/M = 0.7$ to dominating the parameter space at $a/M = 0.99$. The bound region (left of vertical dotted line at $E_0 = 1$) is present at all spins but not relevant for extraction in our baseline impulsive scans, since these initial conditions are bound ($E_0 < 1$) and do not satisfy the escape criterion. High spin ($a/M \gtrsim 0.9$) is essential for practical Penrose extraction.

the spacecraft's prograde orbital velocity in the locally non-rotating frame. The back-of-the-envelope estimate $v_e^{\text{crit}} \approx 0.85\text{--}0.92c$ (depending on periapsis depth and orbital parameters) agrees well with the Monte Carlo observation that success rates remain below $\sim 1\%$ for $v_e \leq 0.90c$ but rise steeply for $v_e \geq 0.93c$. Beyond this onset, Fig. 6 shows η_{cum} approaches a plateau for $a/M = 0.95$, so pushing v_e ever closer to c yields only modest additional gain.

Interestingly, we observe that $a/M = 0.99$ shows *lower* success rates than $a/M = 0.95$ at intermediate velocities ($v_e \leq 0.95c$): at $v_e = 0.90c$, the extreme-spin case achieves 0% success compared to 1% for $a/M = 0.95$ (Tables V–VI). At $v_e = 0.98c$, both spins achieve similarly high success (86–89%; Tables V–VI). Within our maneuver class and steering law, this indicates that pushing the spin closer to extremality does not automatically improve success at fixed v_e , and that the practical optimum depends on the detailed phase-space geometry of escape corridors.

The spin threshold arises from ergosphere geometry: at $a/M = 0.7$, the ergosphere is shallow and the orbit parameter space allowing deep penetration with escape is vanishingly small. The amplification from sweet-spot focusing ($10\times$ to $19\times$) demonstrates that initial condition precision dominates over other factors—a practical challenge for any real mission.

Comparison to electromagnetic extraction mechanisms is instructive. The Blandford–Znajek process [11] achieves sustained extraction through magnetic field lines without requiring ultra-relativistic *material* exhaust, helping contextualize its astrophysical prevalence. Magnetic reconnection in the ergosphere [13] similarly bypasses a material exhaust-velocity threshold by accel-

erating charged particles electromagnetically. Our results are consistent with the view that material-based Penrose extraction, while theoretically elegant, faces severe practical constraints compared with electromagnetic channels in realistic astrophysical settings.

Summary of experimental evidence. The key quantitative findings are organized as follows:

- **Parameter space structure** (Fig. 1): Orbit classification reveals six dynamically distinct regions; the deep ergosphere extraction zone expands from negligible at $a/M = 0.70$ to 44% of parameter space at $a/M = 0.95$.
- **Baseline success rates** (Table I): Broad parameter scans yield Penrose success rates of 0–1.41% across 32,000 trajectories, with no extraction observed for $a/M \leq 0.7$.
- **Spin threshold** (Table II): Practical spin threshold constrained to $0.88 < a_{\text{crit}}/M \lesssim 0.89$ from 140,000 LHS samples.
- **Sweet-spot amplification** (Table III, Fig. 2): Restricting to $(E_0, L_z) \in [1.1, 1.4] \times [2.5, 3.8]$ increases success by $10\times$ to $19\times$.
- **Thrust strategy efficiency** (Table IV, Fig. 3): Single impulse achieves $\eta_{\text{cum}} = 19.2\%$; continuous thrust achieves $\sim 2\%$.
- **Spin dependence** (Fig. 4): Extraction window contracts geometrically with decreasing spin.
- **Velocity phase transition** (Tables V–VI, Fig. 5): Empirical threshold near $v_e \approx 0.91\text{--}0.92c$ for our baseline sweet-spot distribution and thrust policy; peak success 88.5% at $v_e = 0.98c$, $\delta m = 0.4$.

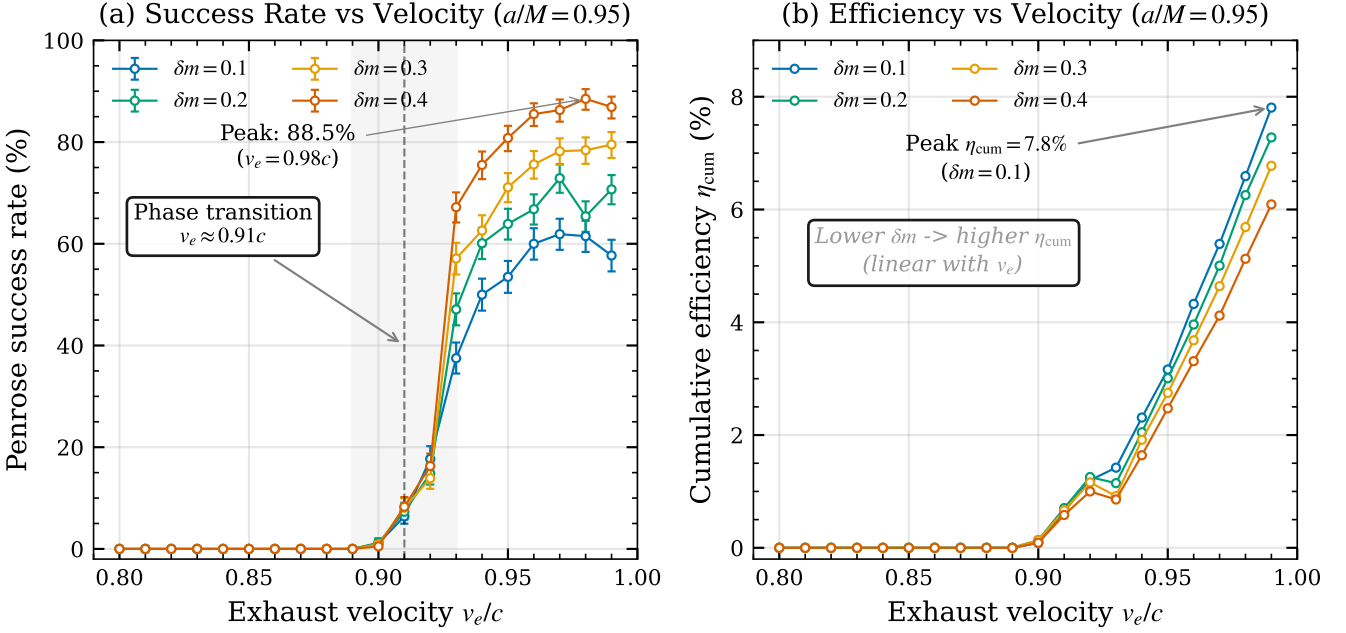


FIG. 5. Thrust parameter sensitivity for $a/M = 0.95$ at the sweet spot ($E_0 = 1.22$, $L_z = 3.05$), sampled at $0.01c$ velocity increments. Each configuration's success rate is computed over 1,000 initial conditions in (E_0, L_z) drawn from a Gaussian distribution centered at $(1.22, 3.05)$ with $\sigma_E = 0.03$, $\sigma_L = 0.08$. (a) Penrose success rate versus exhaust velocity v_e for four ejected mass fractions $\delta m \in \{0.1, 0.2, 0.3, 0.4\}$ with 95% Clopper-Pearson confidence intervals. A sharp onset (rapid transition region) occurs around $v_e \approx 0.91$ – $0.92c$: at $v_e \leq 0.90c$, success is $\lesssim 1\%$ regardless of δm ; above $v_e = 0.93c$, success increases rapidly with both v_e and δm . Peak success of 88.5% achieved at $v_e = 0.98c$, $\delta m = 0.4$. (b) Cumulative efficiency η_{cum} versus exhaust velocity (Eq. 22). Values in panel (b) report the sample mean of η_{cum} over Penrose-successful escapes (conditioning on \mathcal{S}); unsuccessful trajectories are excluded from the efficiency statistic. Cumulative efficiency is *inversely* related to δm : smaller mass fractions yield higher per-mass energy gain. In the range $v_e \in [0.90c, 0.99c]$, efficiency increases approximately linearly with v_e , reaching $\eta_{\text{cum}} = 7.8\%$ at $v_e = 0.99c$, $\delta m = 0.1$. The opposing trends in success rate and efficiency present a design trade-off for practical Penrose propulsion. Figure 6 extends panel (b) to the ultra-relativistic limit $v_e \rightarrow c$.

- *Ultra-relativistic saturation* (Fig. 6): Cumulative efficiency saturates at $\eta_{\text{sat}} \approx 9.1\%$ as $v_e \rightarrow c$.

X. THEORETICAL OPTIMALITY OF SINGLE-IMPULSE EXTRACTION

Our numerical results consistently show that single-impulse thrust outperforms continuous thrust. As the strategy comparison in Sec. IX D indicates, concentrating ejection near periaxis is advantageous; we now provide a simple optimal-allocation argument.

For a *fixed realized trajectory and exhaust-direction schedule*—hence a *fixed profile* $E_{\text{ex}}(\tau)$ along the worldline—the total energy change is:

$$\Delta E = - \int_0^{\tau_f} E_{\text{ex}}(\tau) \cdot \frac{d\mu}{d\tau} d\tau, \quad (62)$$

where $E_{\text{ex}}(\tau)$ is the exhaust Killing energy and $d\mu/d\tau$ is the exhaust rest-mass ejection rate (here μ denotes expelled rest mass, not a spacetime index). For fixed total exhaust mass and fixed $E_{\text{ex}}(\tau)$ profile, maximizing ΔE requires concentrating ejection where E_{ex} is most negative.

Define normalized mass flow $\rho(\tau) = (1/\delta\mu_{\text{total}})(d\mu/d\tau)$ with $\int \rho d\tau = 1$. Then $\Delta E = -\delta\mu_{\text{total}} \langle E_{\text{ex}} \rangle_\rho$, where the path-average satisfies $\langle E_{\text{ex}} \rangle_\rho \geq \min_\tau E_{\text{ex}}(\tau)$. Maximum extraction occurs when $\rho(\tau) = \delta(\tau - \tau^*)$, concentrated at the minimum—precisely a *single impulse* at optimal location.

Caveats. (i) The delta-function optimality assumes no upper bound on instantaneous mass flow; if a constraint $(d\mu/d\tau) \leq \dot{\mu}_{\text{max}}$ is imposed, the optimizer becomes “burn at maximum rate in an interval around τ^* ” rather than a true impulse. (ii) This section proves optimal *allocation* of a fixed fuel budget along a given worldline; global optimality over all steering laws is an optimal-control problem that we do not address here.

The exhaust Killing energy varies with radius: $E_{\text{ex}} \sim 0$ at the ergosphere boundary, ~ -0.1 to -0.2 at $r \sim 1.5M$ (optimal for escape), and more negative at smaller radii (but with increasing capture risk). Continuous thrust averages over this profile, suffering a path-averaging penalty. Additionally, continuous thrust modifies (E, L_z) and the periaxis geometry throughout the ergosphere transit; extended burning can move the spacecraft out of the narrow escape corridor before the maneuver completes, increasing capture probability.

Numerical results confirm this analysis: single im-

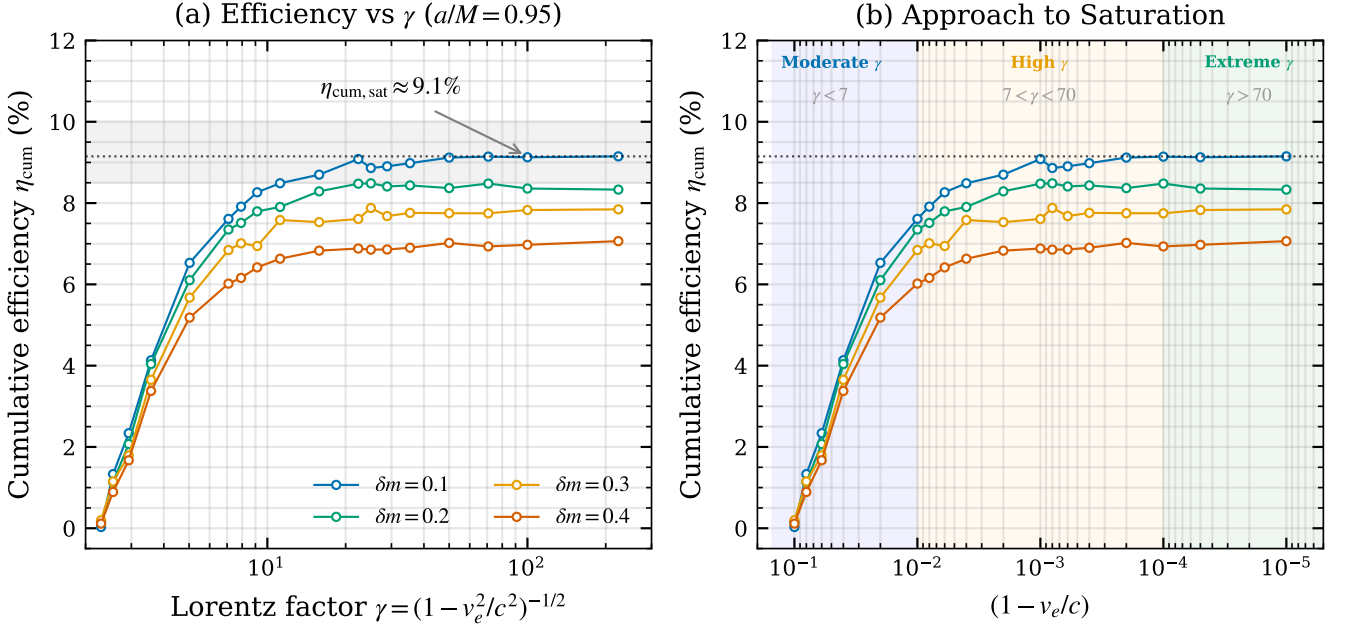


FIG. 6. Continuation of Fig. 5b into the extreme- γ regime for $a/M = 0.95$ in the same sweet-spot region, using the same cumulative efficiency definition (Eq. 22). All η_{cum} values are computed as sample means over Penrose-successful escapes (conditioning on \mathcal{S}). Exhaust velocities are scanned from $v_e = 0.90c$ ($\gamma = 2.3$) to $v_e = 0.99999c$ ($\gamma = 224$). (a) Cumulative efficiency η_{cum} versus exhaust Lorentz factor γ on logarithmic scale. Below $\gamma \approx 10$, η_{cum} grows approximately linearly with γ . Above $\gamma \approx 20$ – 30 , η_{cum} saturates at $\eta_{\text{sat}} \approx 9.1\%$, indicating diminishing returns at this spin parameter. These values are sample means over \mathcal{S} -successful escapes in the Gaussian-sampled sweet spot and should not be confused with the tuned single-impulse optimum reported in Table IV. Lower δm consistently yields higher η_{cum} . (b) η_{cum} versus $(1 - v_e/c)$ showing the approach to saturation. Three regimes are identified: moderate γ ($\gamma < 7$, i.e., $v_e < 0.99c$), high γ ($7 < \gamma < 70$, i.e., $0.99c < v_e < 0.9999c$), and extreme γ ($\gamma > 70$, i.e., $v_e > 0.9999c$). The saturation plateau is approached asymptotically as $v_e \rightarrow c$, with diminishing returns beyond $v_e \approx 0.999c$. This plateau is an empirical ceiling for our baseline sweet-spot distribution and thrust policy, and is not directly comparable to the classic Wald efficiency normalization (20.7% for $a/M \rightarrow 1$).

pulse achieves $\eta_{\text{cum}} \sim 19\%$ with escape, while continuous thrust (escape mode) achieves $\eta_{\text{cum}} \approx 2\%$ (Table IV), consistent with the path-averaging penalty.

Within a fixed escape trajectory, single-impulse Penrose extraction at the E_{ex} minimum represents an upper bound on energy extraction, limited only by geometric constraints and the requirement of eventual escape. This optimality argument does not preclude alternative trajectories with deeper periapsis (and correspondingly more negative E_{ex}), but such trajectories face higher capture risk.

XI. CONCLUSIONS

We have presented a Monte Carlo characterization of the Penrose process using rocket propulsion in Kerr spacetime, framing controlled exhaust as a constrained negative-energy injection problem. Using DOP853 integration ($\text{rtol} = 10^{-10}$, $\text{atol} = 10^{-12}$) for parameter sweeps and forward Euler with mass-shell projection for continuous-thrust trajectories, our study establishes sharp constraints on when extraction succeeds:

1. Even with control, extraction requires fine-

tuning. Only $\sim 1\%$ of trajectories in broad parameter scans achieve both $E_{\text{ex}} < 0$ and escape to infinity. The high success rates attainable under optimal conditions (up to 88.5%) require simultaneously satisfying constraints on spin, exhaust velocity, mass fraction, and initial orbital elements—representing the limiting case of maximum fine-tuning, not generic behavior.

2. High spin is essential. In our baseline sweep and steering law, no successful extractions occur for $a/M \leq 0.88$ ($v_e = 0.95c$, $\delta m = 0.3$; 0/90,000 trajectories), indicating a sharp practical onset near $a/M \approx 0.89$ for this scenario. The critical threshold is constrained to $0.88 < a_{\text{crit}}/M \lesssim 0.89$, with success rates increasing steeply for higher spins.

3. Ultra-relativistic exhaust is required. Within our prograde-flyby family and greedy steering model, a sharp velocity threshold exists near $v_e \approx 0.91$ – $0.92c$, below which extraction largely fails ($\lesssim 1\%$). This threshold arises because the exhaust must overcome the spacecraft's prograde motion to achieve retrograde velocity in the local frame, a condition that becomes geometrically accessible only for sufficiently relativistic ejection.

4. **Single impulse at periapsis is optimal.** Impulsive thrust achieves $\eta_{\text{cum}} \approx 19\%$ (Eq. 22). Continuous thrust achieves only $\sim 2\text{--}4\%$ due to path-averaging over regions where $|E_{\text{ex}}|$ is small (near the ergosphere boundary), reinforcing that timing (not just total thrust) governs efficiency.
5. **Cumulative efficiency saturates in the ultra-relativistic limit.** As $v_e \rightarrow c$ ($\gamma \rightarrow \infty$), cumulative efficiency asymptotically approaches $\eta_{\text{sat}} \approx 9.1\%$ for $a/M = 0.95$ (Fig. 6), with diminishing returns above $v_e \approx 0.999c$.

These constraint results complement prior theoretical analyses of collisional Penrose mechanisms [5, 10] by characterizing the controlled-exhaust regime: even allowing thrust direction and magnitude to vary under our steering prescriptions, the stringent requirements on spin, velocity, and orbital geometry quantify how fine-tuned the Penrose process must be. This fine-tuning is consistent with why electromagnetic mechanisms (Blandford–Znajek, magnetic reconnection) are generally considered the dominant channels for astrophysical energy extraction from rotating black holes, while rocket-propelled extraction remains a limiting idealization.

Engineering summary. To achieve non-negligible Penrose extraction success in our model requires: (i) black hole spin $a/M \gtrsim 0.89$, (ii) exhaust velocity $v_e \gtrsim 0.91c$ (onset around $0.91\text{--}0.92c$), and (iii) initial conditions tuned to the sweet spot $(E_0, L_z) \approx (1.2, 3.0)$. Even then, single-impulse efficiency is capped at $\sim 19\%$ of rocket mass lost, while continuous thrust achieves only $\sim 2\text{--}4\%$. These stringent requirements define the practical boundary of material-based Penrose propulsion.

ACKNOWLEDGMENTS

The authors acknowledge support from the VinUni Center for Environmental Intelligence (CEI).

Appendix A: Numerical Validation

Numerical accuracy was verified through multiple diagnostics. The mass-shell constraint $\mathcal{C} = g^{\mu\nu} p_\mu p_\nu + m^2$ is maintained to $|\mathcal{C}| < 10^{-9}$ for single-impulse trajectories and $< 10^{-6}$ for continuous thrust (with projection restoring $< 10^{-14}$). Future-directedness ($u^t > 0$) and

timelike normalization are verified throughout all trajectories. Energy conservation via 4-momentum balance yields residuals $< 10^{-9}$.

We cross-validated a representative subset of continuous-thrust trajectories with RK45, finding consistent escape/capture outcomes and ΔE within statistical uncertainty. Boyer-Lindquist coordinates become numerically stiff near r_+ ; integration failures (11.2% of samples) occur exclusively for trajectories approaching the horizon ($r < 1.1r_+$), and we conservatively treat such failures as captures. Treating failures as captures yields consistent escape probabilities (Table VIII).

TABLE VII. Simulation accounting breakdown. Main experimental phases (1–4) total 112,000 trajectories; spin-threshold characterization (Phase 5) adds 140,000 LHS trajectories. Fig. 5 uses an additional high-resolution velocity sweep for $a/M = 0.95$ (20 velocities at $0.01c$ increments $\times 4 \delta m \times 1,000 = 80,000$ trajectories) for detailed phase-transition visualization. Parameter sweeps use DOP853 integrator with tolerances $\text{rtol} = 10^{-10}$, $\text{atol} = 10^{-12}$; continuous thrust uses forward Euler with 4-momentum projection.

Phase	Description	Num. Traj.
1	Broad grid (80×80 , 5 spins)	32,000
2	Focused grid (60×60 , 5 spins)	18,000
3	Thrust sensitivity ($4 \times 4 \times 2$ spins $\times 1,000$)	32,000
4	M.C. validation (3 spins $\times 2$ regions $\times 5,000$)	30,000
5	Spin threshold (14 spins $\times 10,000$ LHS)	140,000

TABLE VIII. Conservative Penrose-success rates illustrating the impact of integration failures for representative high-spin cases in a focused sampling domain ($E_0 \in [1.1, 1.3]$, $L_z \in [2.5, 3.5]$) under the periapsis-impulse protocol with $v_e = 0.95c$ and $\delta m = 0.20$. P1: “Penrose (excl. int. failures)” excludes integration failures from the denominator; P2: “Penrose (failures as captures)” counts all failures as non-successes. The differences correspond to the observed $\sim 11.2\%$ failure fraction and support treating integration failures as physical captures near the horizon.

a/M	P1	P2	Diff.
0.90	0.38%	0.33%	-0.05%
0.95	8.34%	7.41%	-0.93%
0.99	10.84%	9.63%	-1.21%

DATA AVAILABILITY

Simulation code is available at https://github.com/anindex/penrose_process. Animated trajectory visualizations are provided in the codebase.

[1] R. Penrose and R. M. Floyd, Extraction of rotational energy from a black hole, *Nature Physical Science* **229**, 177 (1971).

[2] D. Christodoulou, Reversible and irreversible transformations in black-hole physics, *Physical Review Letters* **25**, 1596 (1970).

- [3] J. M. Bardeen, W. H. Press, and S. A. Teukolsky, Rotating black holes: locally nonrotating frames, energy extraction, and scalar synchrotron radiation, *Astrophysical Journal*, Vol. 178, pp. 347-370 (1972) **178**, 347 (1972).
- [4] R. M. Wald, Energy limits on the penrose process, *Astrophysical Journal*, Vol. 191, pp. 231-234 (1974) **191**, 231 (1974).
- [5] T. Piran, J. Shaham, and J. Katz, High efficiency of the penrose mechanism for particle collisions, *Astrophysical Journal Letters* v. 196, p. L107 **196**, L107 (1975).
- [6] M. Bañados, J. Silk, and S. M. West, Kerr black holes as particle accelerators to arbitrarily high energy, *Physical review letters* **103**, 111102 (2009).
- [7] M. Bejger, T. Piran, M. Abramowicz, and F. Håkanson, Collisional penrose process near the horizon of extreme kerr black holes, *Physical review letters* **109**, 121101 (2012).
- [8] E. Berti, R. Brito, and V. Cardoso, Ultrahigh-energy debris from the collisional penrose process, *Physical Review Letters* **114**, 251103 (2015).
- [9] J. D. Schnittman, Revised upper limit to energy extraction from a kerr black hole, *arXiv preprint arXiv:1410.6446* (2014).
- [10] E. Leiderschneider and T. Piran, Maximal efficiency of the collisional penrose process, *Physical Review D* **93**, 043015 (2016).
- [11] R. D. Blandford and R. L. Znajek, Electromagnetic extraction of energy from kerr black holes, *Monthly Notices of the Royal Astronomical Society* **179**, 433 (1977).
- [12] A. Tchekhovskoy, R. Narayan, and J. C. McKinney, Efficient generation of jets from magnetically arrested accretion on a rapidly spinning black hole, *Monthly Notices of the Royal Astronomical Society: Letters* **418**, L79 (2011).
- [13] L. Comisso and F. A. Asenjo, Magnetic reconnection as a mechanism for energy extraction from rotating black holes, *Physical Review D* **103**, 023014 (2021).
- [14] S. Koide and K. Arai, Energy extraction from a rotating black hole by magnetic reconnection in the ergosphere, *The Astrophysical Journal* **682**, 1124 (2008).
- [15] S. Chandrasekhar and K. S. Thorne, The mathematical theory of black holes (1985).
- [16] M. Bhat, S. Dhurandhar, and N. Dadhich, Energetics of the kerr-newman black hole by the penrose process, *Journal of Astrophysics and Astronomy* **6**, 85 (1985).
- [17] C. J. Clopper and E. S. Pearson, The use of confidence or fiducial limits illustrated in the case of the binomial, *Biometrika* **26**, 404 (1934).
- [18] B. Efron, Better bootstrap confidence intervals, *Journal of the American statistical Association* **82**, 171 (1987).